International Journal of Heat and Fluid Flow 97 (2022) 109036

Contents lists available at ScienceDirect

International Journal of Heat and Fluid Flow

journal homepage: www.elsevier.com/locate/ijhff

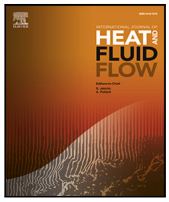

Control effects on coherent structures in a non-uniform adverse-pressure-gradient boundary layer

Marco Atzori [a,*], Ricardo Vinuesa [b], Philipp Schlatter [b]

[a] Department of Particulate Flow Modelling, Johannes Kepler University, Linz, 4040, Austria
[b] SimEx/FLOW, Engineering Mechanics, KTH Royal Institute of Technology, Stockholm, 10044, Sweden

ARTICLE INFO

MSC:
0000
1111

Keywords:
Turbulent boundary layers
Flow control
Coherent structures

ABSTRACT

We examine the effects of three basic but effective control strategies, namely uniform blowing, uniform suction, and body-force damping, on the intense Reynolds-stress events in the turbulent boundary layer (TBL) developing on the suction side of a NACA4412 airfoil. This flow is subjected to a non-uniform adverse pressure gradient (APG), which substantially modifies its turbulence statistics with respect to a zero-pressure-gradient (ZPG) boundary layer, and it also changes how control strategies affect the flow. The strong APG results in intense events that are shorter and more often detached from the wall than in ZPG TBLs. In a quadrant analysis, ejections remain the most relevant structures, but sweeps become more important than in ZPG TBLs, a fact that results in a lower contribution to the wall-normal velocity from intense Reynolds-stress events. Control effects are relatively less important on intense events than on the turbulent statistics. Uniform blowing has an impact similar to that of an even more intense APG, while uniform suction has more complex effects, most likely due to the particular behavior of the wall-normal velocity component near the wall. Body-force damping also reduces the probability of occurrence of very-large attached structures and that of intense events in the proximity of the actuation region. Our results show that intense Reynolds-stress events are robust features of the flow. If control strategies do not target directly these structures, their effects on the strong events is less pronounced than the effects on the mean flow.

1. Introduction

Uniform blowing and suction have been considered as possible control strategies to modify the properties of turbulent flows for more than a century (see Prandtl (1904)). In the case of uniform blowing, the possibility of obtaining skin-friction reduction in industrial cases became more concrete with the introduction of the micro-blowing technique (as discussed by Hwang (2004)), prompting several studies on the interaction between control and turbulence. These studies focused initially on canonical cases, such as zero-pressure-gradient (ZPG) turbulent boundary layers (TBLs) (*e.g.* Park and Choi (1999), Kametani and Fukagata (2011), and Stroh et al. (2016)). Only recently, however, detailed analyses have been carried out on blowing and suction effects for more complex cases, closely related to aerodynamics applications. These studies are based on both experiments, as in the cases of *e.g.* Eto et al. (2019) and Kornilov et al. (2019), and numerical simulations, as in the cases of *e.g.* Atzori et al. (2020) and Fahland et al. (2021). A key distinction between these more recent studies and the previous ones is the fact that turbulent boundary layers developing around wing profiles are often subjected to pressure gradients, and most notably intense adverse pressure gradient (APG).

Turbulent boundary layers subjected to strong APG exhibit specific features compared with the canonical ZPG case. For a similar development length, APG TBLs are thicker, have higher mean wall-normal convection and more intense turbulent fluctuations in the outer region, as shown in numerous numerical and experimental studies (*e.g.* Spalart and Watmuff (1993), Skåre and Krogstad (1994), and Monty et al. (2011)). Furthermore, the state of the flow is not uniquely determined by the local pressure condition, but it results from the pressure distribution during its development (Bobke et al., 2017). Significant differences between APG and ZPG TBLs are also apparent in how control strategies affect both flows. For instance, Atzori et al. (2020) described the effects of uniform blowing and uniform suction on the suction side on the non-uniform APG TBL developing on the suction side of a NACA4412 airfoil and found that blowing effects on wall-normal convection and turbulent fluctuations are more pronounced than in ZPG TBLs.

A possible approach to untangle the complexity of pressure-gradient effects is to describe their impact on coherent structures that are relevant for near-wall dynamics. Maciel et al. (2017b) studied Reynold-stress events in TBLs with APG of various intensities, showing that

* Corresponding author.
E-mail address: marco.atzori@jku.at (M. Atzori).

https://doi.org/10.1016/j.ijheatfluidflow.2022.109036
Received 20 February 2022; Received in revised form 4 July 2022; Accepted 22 July 2022
Available online 8 August 2022

Table 1
Cases examined in the present study.

Case	Description	Control region	Color
PREF	Reference ZPG case, pressure side	–	
SREF	Reference APG case, suction side	–	
BLW	Uniform blowing ($0.1\%U_\infty$), suction side	$0.25 < x/c < 0.86$	
SCT	Uniform suction ($0.1\%U_\infty$), suction side	$0.25 < x/c < 0.86$	
BDF	Body-force damping, suction side	$0.25 < x/c < 0.86$	

large wall-attached objects are less relevant in stronger APG conditions, which cause them to become less common and shorter in the wall-tangential direction. This approach was introduced by Lozano-Durán et al. (2012) as extension of the classical quadrant analysis (Wallace et al., 1972). Atzori et al. (2019) conducted a preliminary study on the same coherent structures on a NACA4412 airfoil, focusing on their contributions to wall-normal convection and found that ejections and sweeps have more similar intensities in APG TBLs than in ZPG TBLs and internal flows such as channel and duct.

In the present paper, we study how three different control strategies, namely uniform blowing, uniform suction, and body-force damping applied to the APG TBL on the suction side of a NACA4412 airfoil affect intense Reynolds-stress events. In particular, we are interested in understanding how a specific control strategy affects the dominant coherent structures in the flow. Since these structures are relevant to the near-wall regeneration cycle, better understanding of the control effects may help developing more efficient control strategies.

The paper is organized as follows: in Section 2, we describe the data set and structure detection technique; in Section 3, we examine the geometrical properties of coherent structures, including their size, shape, and distribution with respect to the wall-distance, their probability of occurrence, and their contribution to the mean flow; and in Section 4, we summarize our findings and present our conclusions.

2. Methodology

2.1. Data set

The data set that we consider is a subset of that described in detail in Ref. Atzori et al. (2020), which consists of highly-resolved large-eddy simulations (LES) of the incompressible flow around a NACA 4412 airfoil at chord Reynolds number $Re_c = 200,000$ and angle of attack 5 degrees performed with the spectral-element code Nek5000 (Fischer et al., 2008). Note that $Re_c = U_\infty c/\nu$, where U_∞ is the incoming velocity, c is the chord length, and ν is the kinematic viscosity. In these simulations, we induce laminar-to-turbulent transition with tripping at $x_1/c = 0.1$ on both sides of the airfoil, and control techniques are applied on a portion of the suction side. The horizontal and vertical coordinates in the computational domain are denoted by x_1 and x_2, respectively (the airfoil is horizontal and incoming velocity components define the angle of attack), while the wall-tangential, wall-normal, and spanwise directions are denoted by x, y, and z, respectively.

The grid spacing is $\Delta x^+ \approx 18$, $\Delta y^+ = (0.64, 11)$, and $\Delta z^+ \approx 9$ for the wall-tangential, wall-normal and spanwise directions, respectively. Note that the superscript $(\dots)^+$ denotes inner-scaled variables and the inner scaling is computed using the viscous local length $l^\star = \nu/u_\tau$, where the friction velocity is $u_\tau = \sqrt{\tau_w/\rho}$, the wall-shear stress at the wall is $\tau_w = \rho\nu(\mathrm{d}U/\mathrm{d}y)_{y=0}$, and ρ is the fluid density.

In the present paper, in order to isolate adverse-pressure-gradient and control effects, we focus on only a portion of the domain and a limited set of cases. The five selected study cases are listed in Table 1. The two first cases, denoted PREF and SREF, respectively, are regions of pressure and suction sides of the reference case. Note that the boundary layer on the pressure side is subjected to a mild favorable pressure gradient. The remaining three cases, denoted BLW, SCT, and BDF, respectively, are regions of the suction side of the simulations with uniform blowing, uniform suction, and body-force damping. Uniform blowing and uniform suction are implemented as a Dirichlet boundary condition on the airfoil surface, prescribing a wall-normal velocity of $0.1\%U_\infty$ in the appropriate direction. Body-force damping is implemented as a volume force opposite to the wall-normal component of the instantaneous velocity in the region below $y^+ < 20$, similarly to that used by Stroh et al. (2015), and it is calibrated to yield a skin-friction reduction comparable to that of uniform blowing. Note that, for this specific test case, a blowing intensity of $0.2\%U_\infty$ is already sufficient to cause separation at the trailing edge (Atzori et al., 2020).

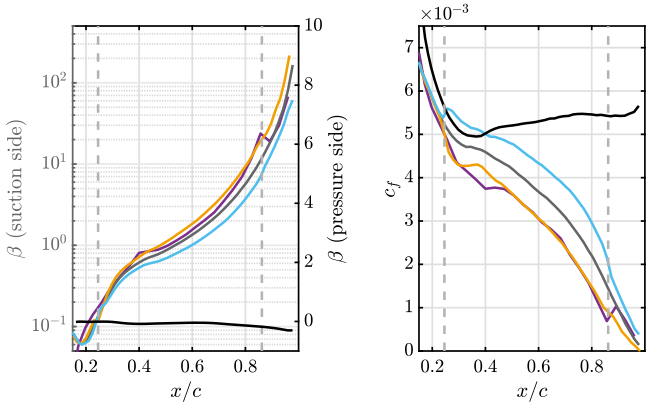

Fig. 1. Development of the boundary layer, described by (left) the Clauser pressure-gradient parameter, denoted by β, and (right) the local skin-friction coefficient, denoted by c_f. Color code described in Table 1. Note that the left axis on the β plot is referred to the curves for the suction side, and the right axis is referred to the curve on for the pressure side. The gray vertical dashed lines denote the control region. (For interpretation of the references to color in this figure legend, the reader is referred to the web version of this article.)

The local skin-friction coefficient, denoted by c_f, and the Clauser pressure-gradient parameter, denoted by β, are shown in Fig. 1 for all the cases. Note that the skin-friction coefficient and the Clauser parameter are defined as $c_f = 2\tau_w/\rho U_e^2$ and $\beta = \delta^*/\tau_w \mathrm{d}P/\mathrm{d}x|_e$, respectively. In these expressions, U_e is the mean wall-tangential velocity at the boundary-layer edge, $\mathrm{d}P/\mathrm{d}x|_e$ is the mean wall-tangential pressure gradient at the boundary-layer edge, and δ^* is the displacement thickness. The location of the edge is identified using the method based on diagnostic plot proposed by Vinuesa et al. (2016), avoiding arbitrary thresholds or identification of maxima in the profiles.

On the suction side, β is positive and after the location of maximum camber ($x/c = 0.4$) rapidly increases, reaching values higher than 100 at the airfoil trailing edge in the reference case. On the pressure side, β exhibits much less conspicuous variations than on the suction side, and it varies between approximately -0.1 at $x/c = 0.4$ and -0.2 at $x/c = 0.8$. The control strategies that we consider slightly alter β, because of their effects on friction velocity and boundary-layer thickness. Uniform blowing increases δ^* and reduces u_τ, leading to higher β, while suction has the opposite effects. Body-force damping also causes an increase of β, which is more evident in the controlled region with already high adverse pressure gradient. In the test cases considered here, the strong adverse pressure gradient on the suction side causes the skin friction to rapidly decrease approaching the leading edge, almost reaching mean separation. Uniform blowing with this actuation intensity causes an integrated skin-friction reduction of approximately 10% and uniform suction causes an increase of the same proportion.

2.2. Coherent structure identification

We define coherent structures as connected components of the domain where the condition below is fulfilled, following the three-dimensional extension of the quadrant analysis proposed in Ref.

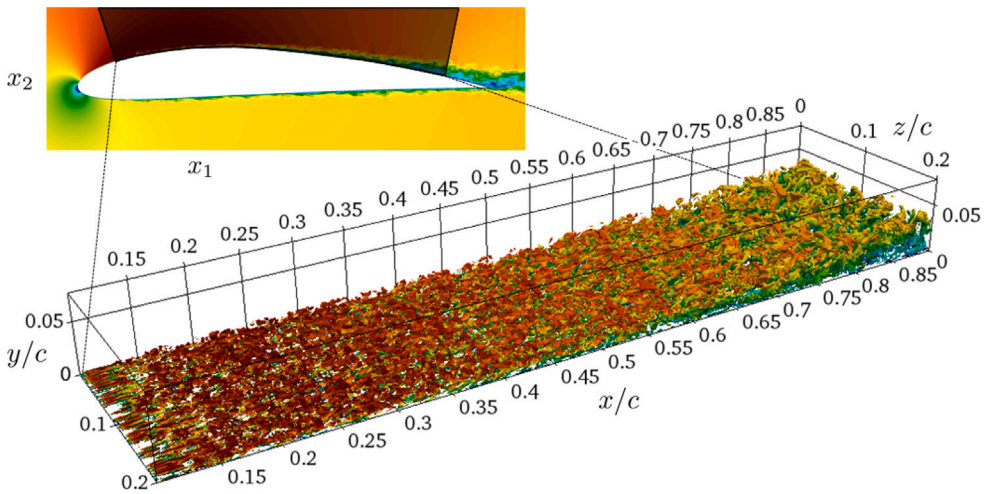

Fig. 2. (Top) Instantaneous horizontal velocity component in the streamwise direction in a portion of the computational domain and (bottom) coherent structures on the suction side of the uncontrolled case in the rotated frame of reference employed in this paper. The coherent structures are colored with wall-tangential velocity component. For both figures, the velocity values are from (blue) $-0.2U_\infty$ to (red) $1.5U_\infty$, approximately. (For interpretation of the references to color in this figure legend, the reader is referred to the web version of this article.)

(Lozano-Durán et al., 2012):

$$|uv| > Hu_{\rm rms}v_{\rm rms}\,. \tag{1}$$

In this expression, u and v are the fluctuations of the wall-tangential, and wall-normal velocity components, respectively, $u_{\rm rms}$ and $v_{\rm rms}$ are the corresponding root-mean-squared values, which are used as scaling factors, and H is a numerical threshold. Note that the simulations are performed using a Cartesian reference frame, but the coherent-structure identification is carried out in a non-orthogonal frame of reference using the wall-tangential and wall-normal directions, and the velocity components are rotated accordingly. Fig. 2 illustrates a small portion of the computational domain in the simulation, and the coherent structures identified in the rotated frame of reference for the uncontrolled case on the suction side. It is possible to appreciate the tripping effects, at $x/c \approx 0.1$, and the rapid growth of the boundary layer due to the APG.

We performed this analysis in a preliminary study on cases PREF and SREF (Atzori et al., 2019), and we observed that the sole condition (1) is not entirely appropriate for this kind flow because above the turbulent–non-turbulent-interface (TNTI), $u_{\rm rms}$ and $v_{\rm rms}$ are virtually zero, resulting in the detection of very large structures, the sizes of which were are almost independent of H in this region. A similar effect has also been observed in the near-wall region in wall-bounded turbulent flows such as that across periodic channels and ducts (Atzori et al., 2021a). Atzori et al. (2019) considered three different additional conditions to identify the turbulent region. Although they are based on different physical quantities, such as enstrophy and turbulent kinetic energy, all these criteria require an additional numerical threshold, and we found that the impact of these conditions on structure identification is similar if the averaged TNTI is the same. In the present study, we restrict the structure identification to regions of the domain where the instantaneous turbulent kinetic energy, defined as

$$\tilde{k} = \frac{1}{2}(u^2 + v^2 + w^2)\,, \tag{2}$$

is higher than a fraction of the turbulent kinetic energy at the boundary-layer edge, defined as

$$k_e = \frac{1}{2}(\overline{u_e^2} + \overline{v_e^2} + \overline{w_e^2})\,. \tag{3}$$

In this expression, the subscript e denotes the location of the edge. We will consider intense events that are detected with $H = 2$, in the region where the instantaneous turbulent kinetic energy, $\tilde{k}$, is at least 2% of the mean turbulent kinetic energy at the edge, k_e, so that the complete condition for structure identification is summarized in following expression:

$$\begin{cases} |uv| > Hu_{\rm rms}v_{\rm rms} \\ \tilde{k} > \alpha k_e \end{cases} \tag{4}$$

The value of the threshold $H = 2$ guarantees that the intense events are isolated and $\alpha = 2\%$ results in an averaged wall-normal distance of the TNTI in good agreement with δ_{99}.

The effects of the two conditions in Eq. (4) are separately illustrated for the plane perpendicular to the streamwise direction at $x/c = 0.75$ for an arbitrary time in Fig. 3.

The top panel shows regions of intense uv events for four progressively higher values of H. The first two, $H = 0.1$ and 0.2, are lower than the value corresponding to the percolation crisis, so that most structures are merged in very large connected components. The higher two, $H = 1$ and 2, are above the critical value, where the most intense events are well separated. The central panel shows the turbulent region of the domain, defined in terms of various percentage of the mean turbulent kinetic energy at the edge of the boundary layer, from $\tilde{k} = 0.1\%k_e$ to $2\%k_e$. The bottom panel shows the instantaneous wall-tangential velocity component, coherent structures and TNTI, for the threshold values employed in this study, which correspond to the highest value considered in the previous panels. Comparing the three panels, it is possible to observe that the TNTI condition has a relatively small impact on the identification of very intense events, which are the focus of this study.

3. Results

In this section, we discuss how control strategies and APGs affect the coherent structures that we identify, considering their geometrical properties as well as their probability of occurrence and relation with wall-normal convection. We focus on the portion of the domain between $x/c = 0.4$ and $x/c = 0.8$, corresponding to the region of adverse pressure gradient on the suction side, far enough from both transition location and trailing edge.

3.1. Geometrical properties of the structures

3.1.1. Structure size

We first examine the structure sizes in the entire sub-domain for each case, in order to identify the most evident trends. Fig. 4 illustrates

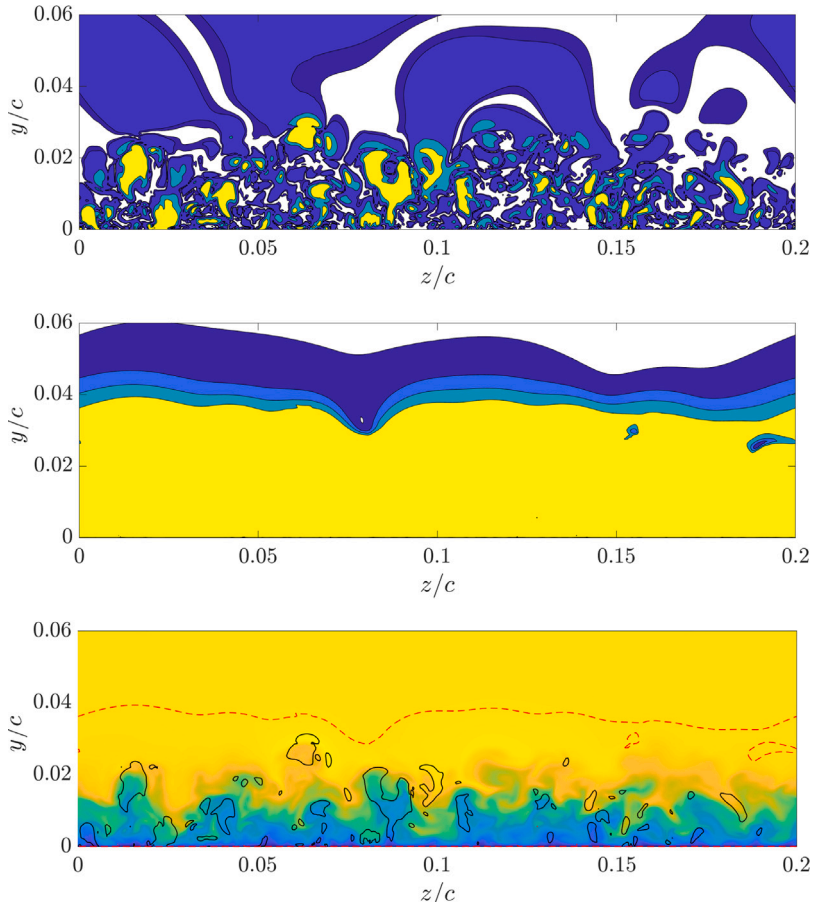

Fig. 3. Effects of the two thresholds employed in structure identification, illustrated for the plane $x/c = 0.75$ at an arbitrary time. (Top) Regions of space identified with the condition $|uv| > Hu_{\mathrm{rms}}v_{\mathrm{rms}}$ for $H = 0.1$, 0.2, 1, and 2, denoted by dark blue, light blue, cyan, and yellow, respectively. (Center) Regions of space where the turbulent kinetic energy is higher than 0.1%, 0.5%, 1%, and 2% of the mean turbulent kinetic energy at the edge, denote by dark blue, light blue, cyan, and yellow, respectively. (Bottom) Wall-tangential velocity component with values from $\approx 0U_\infty$, in blue, to $\approx 1.2U_\infty$, in yellow, contours of intense uv for $H = 2$, denoted by solid black lines, and region where the structures are identified, denoted by dashed red lines. (For interpretation of the references to color in this figure legend, the reader is referred to the web version of this article.)

the probability density functions (PDFs) of the lengths in every direction of the structure bounding boxes, denoted by Δ_x, Δ_y, and Δ_z. The lengths are scaled both with δ_{99} and in viscous units, using δ_{99} and $l^\star$ at the streamwise location of the structure center of mass, denoted by x_{cm}. Note that the center of mass, $\boldsymbol{x}_{\mathrm{cm}}$, is defined as:

$$\boldsymbol{x}_{\mathrm{cm}} = \frac{1}{\mathcal{V}} \sum_{i=1}^{\mathcal{N}} \mathcal{V}_i \boldsymbol{x}_i \,, \tag{5}$$

where $\boldsymbol{x}_i$ is position of the ith point belonging to the structure, $\mathcal{V}_i$ is the portion of domain volume associated with this grid point, which is computed using the grid spacing and mesh curvature, $\mathcal{N}$ is the total number of points belonging to the structure, and $\mathcal{V} = \sum_{i=1}^{\mathcal{N}} \mathcal{V}_i$ is the structure volume.

Generally speaking, pressure-gradient effects on the structure sizes are more evident than control effects, which is not surprising because the APG is relatively strong, and the control actuation is relatively weak. We will now compare the suction and pressure sides in the reference case (cases SREF and PREF, respectively).

With respect to the boundary-layer thickness, the APG results in structures that are on average smaller on the suction side (SREF) than on the pressure side (PREF), which is apparent in the PDFs of the bounding-box size in all directions. For example, very large structures in PREF can be as long as 10 times δ_{99} and beyond but the longest ones in SREF are shorter than that. Intense events in PREF are also more elongated in the vertical and spanwise directions than in SREF, indicating that although the APG increases the boundary-layer thickness, the size of intense events does not grow proportionally. When the lengths are scaled in viscous units, APG effects are less evident. The length in the streamwise direction, Δ_x^+, is still shorter on average on the suction side than on the pressure side, but Δ_z^+ is more similar between both and Δ_y^+ is virtually identical.

Control effects are less significant than those of the pressure gradient, but it is still possible to identify general trends. Uniform blowing (BLW) modifies certain turbulence statistics similarly to an even stronger APG, and uniform suction (SCT) has opposite effects (Vinuesa et al., 2017; Atzori et al., 2020). We observe the same in how these control strategies affect the structure sizes. For instance, Δ_x/δ_{99} and Δ_z/δ_{99} are on average slightly lower in BLW than in the uncontrolled case. However, control effects on Δ_y/δ_{99} are so small that the corresponding PDFs overlap for all cases on the suction side. Interestingly, although pressure-gradient effects are less evident when the lengths are scaled in viscous units, we observe the opposite for blowing and suction effects. For example, the Δ_z/δ_{99} PDFs in SREF and SCT are overlapping, but Δ_z^+ in SCT is, in fact, more similar to that on the pressure side than for the uncontrolled cases. To summarize, structure sizes scaled in viscous units are relatively in better agreement between APG and ZPG than between blowing, suction, and the uncontrolled case, while sizes scaled with δ_{99} are in better agreement between blowing, suction and the uncontrolled case than between APG and ZPG. This fact suggests the blowing and suction, compared to pressure gradient, modify friction proportionally more than structure sizes in a turbulent boundary layer.

The effects of body-force damping on the average structure sizes are to very slightly increasing Δ_x/δ_{99}, leaving Δ_y/δ_{99} and Δ_z/δ_{99} almost unchanged. Interestingly, Δ_x^+ in BDF is in excellent agreement with

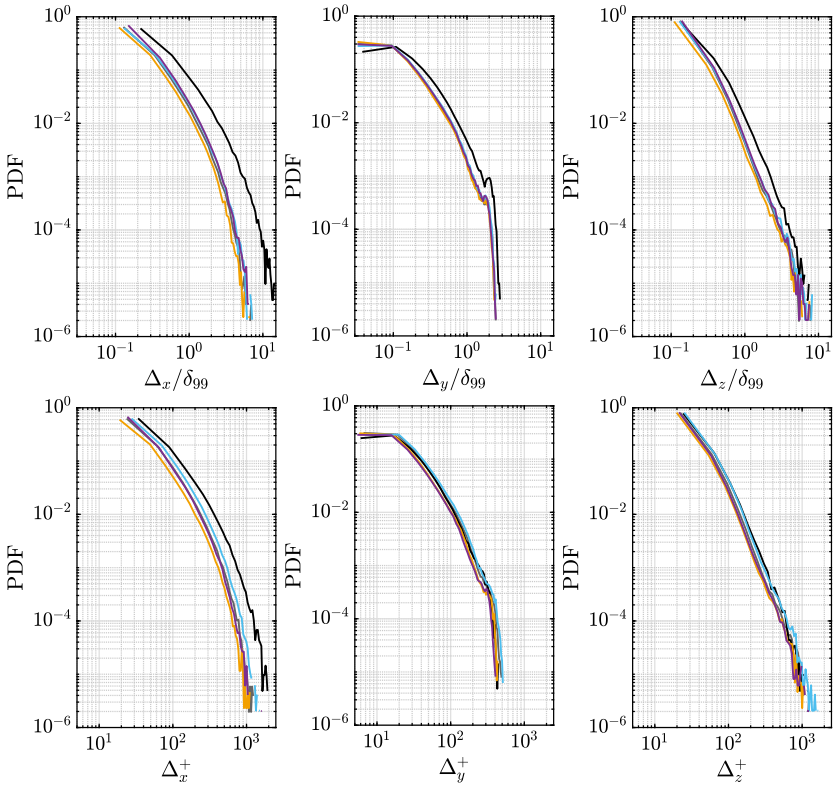

Fig. 4. Size of the bounding boxes of structures, scaled in (top row) outer and (bottom row) viscous units. From left to right, dimensions in streamwise, wall-normal and spanwise directions. Color code described in Table 1. (For interpretation of the references to color in this figure legend, the reader is referred to the web version of this article.)

that of the uncontrolled case, showing that this control modifies skin-friction and coherent structures length proportionally, in contrast with uniform blowing.

3.1.2. Vertical placement and extent

Perhaps the most prominent feature of the spatial distribution of intense uv events in wall-bounded flows is the presence of very large structures which extend from the near-wall region (below $y^+ \approx 20$) up to the wake region of the boundary layer. These structures have been observed *e.g.* in channel flows at relatively high Reynolds number (Lozano-Durán et al., 2012) as well as turbulent boundary layers (Maciel et al., 2017a). Their existence is shown by the joint probability density function (JPDF) of the minimum and maximum distance from the wall of the structures, which is reported in Fig. 5 for all cases. Note that the figure illustrates two levels of the JPDF, corresponding to 90% and 99% of the detected structures so that the latter also includes very rare events. The distance from the wall is scaled in local viscous units or δ_{99}, computed at the streamwise location of the structure center of mass. Large objects attached to the wall and propagating at a higher wall-normal distance belong to the thin band with low $y_{\min}$ and high $y_{\max}$, which is present in all cases. An interesting feature of these JPDFs for turbulent boundary layers is the existence of very rare events whose $y_{\max}$ is higher than the $y_{\min}$ of any other, implying that they extend above the region where intense fluctuations can originate, *i.e.* at a distance from the wall as high as $2\delta_{99}$ and more. These coherent structures, the boundaries of which coincide with the TNTI, are equivalent in boundary layers to the largest objects in internal flows, which span the entire domain height. Similar events seem to appear in a similar JPDF for $y_{\min}/\delta_{99}$ and $y_{\max}/\delta_{99}$ reported for an APG boundary layer by Maciel et al. (2017a), although this data set is not directly comparable with the present one because no additional condition was used to exclude the region above the TNTI in Ref. (Maciel et al., 2017a).

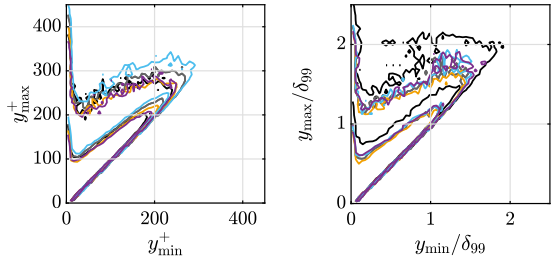

Fig. 5. Joint probability density functions (JPDFs) of the minimum and maximum distance of each structure (left) in inner units and (right) scaled with δ_{99} at the location of structure center of mass. The contours include 90% and 99% of the detected structures. Color code described in Table 1. (For interpretation of the references to color in this figure legend, the reader is referred to the web version of this article.)

3.1.3. Probability of appearance

To quantify how pressure gradient and control modify the probability of occurrence of large events, we establish criteria to classify intense events. These criteria are based on the structure position with respect to the near-wall region, defined as the domain portion below $y^+ = 20$. Coherent structures, which are partially included in the near-wall region with center of mass located above $y^+ = 20$, are included in the tall-wall-attached class, denoted by TWA; structures with center of mass below $y^+ = 20$ are included in the wall-attached class, denoted by WA; and structures that are entirely above the near-wall region are included in the detached class, denoted by D. Table 2 summarizes the number of events in each class for all cases, as well as the corresponding portion of the total volume, between streamwise locations $x/c = 0.75$ and $x/c = 0.85$. In this table, N_{tot} denotes the total number of structures identified in the data set, and N_{class} denotes the number of structures of a specific class, so that $N_{\text{class}}/N_{\text{tot}}$ is the probability of occurrence. Similarly, $\mathcal{V}_{\text{tot}}$ and $\mathcal{V}_{\text{class}}$ denote the total volume occupied by all structures and the

Table 2
Relative probability of occurrence and volume fraction for tall wall-attached (TWA), wall-attached (WA), and detached (D) structures. N_{tot} denotes the total number of structures identified in the data set, and N_{class} denotes the number of structures of a specific class, so that N_{class}/N_{tot} is the probability of occurrence. Similarly, $\mathcal{V}_{tot}$ and $\mathcal{V}_{class}$ denote the total volume occupied by all structures and the volume of structures belonging to a specific class, respectively, so that $\mathcal{V}_{class}/\mathcal{V}_{tot}$ is the volume fraction. The highest values of N_{class}/N_{tot} and $\mathcal{V}_{class}$ for each case is in boldface.

	N_{class}/N_{tot}				
	PREF	SREF	BLW	SCT	BDF
TWA	16%	12%	11%	13%	12%
WA	28%	27%	28%	25%	28%
D	**56%**	**61%**	**61%**	**62%**	**60%**
	$\mathcal{V}_{class}/\mathcal{V}_{tot}$				
	PREF	SREF	BLW	SCT	BDF
TWA	**66%**	**56%**	**51%**	**54%**	**50%**
WA	3%	3%	3%	3%	4%
D	31%	41%	46%	43%	46%

volume of structures belonging to a specific class, respectively, so that $\mathcal{V}_{class}/\mathcal{V}_{tot}$ is the volume fraction.

We observe that pressure gradient and control affect the probability of occurrence and structures volume differently. In all cases, the most numerous class is that of D objects, which includes 56% of the intense events on the pressure side. On the other hand, the class that amounts for the largest portion of the domain is that of TWA objects, which includes for instance on the pressure side 66% of the total volume. The adverse pressure gradient on the suction side results in a lower occurrence of TWA structures (−4%) and a corresponding lower portion of the volume (−10%). This is mainly counterbalanced by an increase in both number and portion of the volume of D intense events (+5% and +10%, respectively), while WA events are very similar in number and volume fraction on both pressure and suction sides.

Interestingly, the control strategies have a relatively small effect on the probability of occurrence, and the most significant discrepancy with respect to the uncontrolled case is a reduction of 2% of the occurrence of WA structure in the case of suction. However, control effects are more evident in the volume fraction of different classes. In particular, both uniform blowing and body-force damping result in lower $\mathcal{V}_{TWA}/\mathcal{V}_{tot}$ (−5% and −6%, respectively) and higher $\mathcal{V}_{D}/\mathcal{V}_{tot}$ (+5% in both cases); uniform suction, perhaps surprisingly, also results in lower $\mathcal{V}_{TWA}/\mathcal{V}_{tot}$ (−2%) and higher $\mathcal{V}_{D}/\mathcal{V}_{tot}$ (+2%), although these are still lower modifications than for blowing.

The reduction of both N_{TWA}/N_{tot} and $\mathcal{V}_{TWA}/\mathcal{V}_{tot}$ due to APG, the further reduction of $\mathcal{V}_{TWA}/\mathcal{V}_{tot}$ due to uniform blowing, and the corresponding increase of N_{D}/N_{tot} and $\mathcal{V}_{D}/\mathcal{V}_{tot}$, are most likely consequences of the higher wall-normal convection associated with both APG and blowing, which causes large structures to move farther from the wall while they are growing in size. The fact that N_{WA}/N_{tot} and $\mathcal{V}_{WA}/\mathcal{V}_{tot}$ are not proportionally affected is probably because these smaller structures have a short lifetime and their rate of production in the near-wall region is not severely affected by either APG or blowing. The fact that suction effects on the volume fractions are in the same direction as those of blowing, albeit less intense, is notable and more intriguing. A possible explanation for this phenomenon is the fact that not only suction reduces the wall-normal convection far from the wall, which should have led to *e.g.* higher $\mathcal{V}_{TWA}/\mathcal{V}_{tot}$, but it also creates a small near-wall region where the wall-normal velocity is negative, hindering the transformation of WA into TWA structures.

3.2. Quadrants and contributions to wall-normal convection

Intense Reynolds-stress events can also be classified considering the signs of velocity fluctuations, which is the basis of the so-called quadrant analysis (Wallace et al., 1972; Willmarth and Lu, 1972). If coherent structures are represented in a Cartesian plane where the horizontal and vertical axes are the wall-tangential and wall-normal fluctuations of the velocity components, respectively, it is possible to assign each of them into one of four quadrants: Q1, ($u > 0$ and $v > 0$), Q2 ($u < 0$ and $v > 0$), Q3 ($u < 0$ and $v < 0$), and Q4 ($u > 0$ and $v < 0$). The most relevant events in wall-bounded flows are Q2 and Q4 events, which are conventionally named ejections and sweeps, respectively. Note that, because of the relatively high value of the threshold ($H = 2$) and the boundary-layer geometry, velocity fluctuations have homogeneous signs within each structure, so the quadrant classification is unambiguous.

Table 3
Relative probability of occurrence and volume fraction for the four quadrants.

	N_Q/N_{tot}				
	PREF	SREF	BLW	SCT	BDF
Q1	12%	14%	15%	13%	15%
Q2	**32%**	**35%**	**34%**	**35%**	**33%**
Q3	22%	17%	17%	18%	20%
Q4	**34%**	**34%**	**34%**	**34%**	**32%**
	$\mathcal{V}_Q/\mathcal{V}_{tot}$				
	PREF	SREF	BLW	SCT	BDF
Q1	2%	2%	1%	2%	2%
Q2	**81%**	**72%**	**69%**	**72%**	**71%**
Q3	5%	6%	8%	7%	7%
Q4	12%	20%	22%	19%	20%

In Table 3, we report the probability of occurrence and volume fractions of different quadrants, denoted by N_Q/N_{tot} and $\mathcal{V}_Q/\mathcal{V}_{tot}$, respectively, in the region between $x/c = 0.75$ and $x/c = 0.85$. In all cases, the number of ejections is very similar to that of sweeps, and their relative proportion does not change significantly between both suction and pressure sides or between controlled and uncontrolled cases. In particular, N_{Q2}/N_{tot}, which is 32% in PREF, increases only by 3 percentage points, because of the APG, and $N_{Q4}/N_{tot} = 34\%$ for every cases expect in BDF, where it still is 32%. Note that ejections and sweeps are statistically coupled in pairs entangled with vortex clusters (del Álamo et al., 2006; Lozano-Durán et al., 2012), which is the reason why N_{Q2}/N_{tot} and N_{Q4}/N_{tot} have similar values. This fact is possibly related to the observation that the probabilities are not much affected by APG or the types of control considered here, because they appear to be a general characteristic of this kind of flow.

The importance of ejections relative to the other quadrants is evident in their volume fractions $\mathcal{V}_Q/\mathcal{V}_{tot}$, which are much higher than the volume fractions of any other quadrants in all cases. Interestingly, the APG modifies both $\mathcal{V}_{Q2}/\mathcal{V}_{tot}$ and $\mathcal{V}_{Q4}/\mathcal{V}_{tot}$ quite significantly, decreasing the first from 81% to 72%, and increasing the second from 12% to 20%, which are more evident changes than those of the probabilities of occurrence. The fact that a strong APG boundary layer has proportionally larger sweeps than ejections with respect to a ZPG boundary layer, although their probability of occurrence is in good agreement in both cases, suggests that these structures are originated similarly, but their evolution is different. The control strategies have a smaller impact on $\mathcal{V}_Q/\mathcal{V}_{tot}$. As observed for TWA and D objects, uniform blowing changes the quadrant volume fractions in the same direction as the adverse pressure gradient does, further decreasing $\mathcal{V}_{Q2}/\mathcal{V}_{tot}$ and increasing $\mathcal{V}_{Q4}/\mathcal{V}_{tot}$, but uniform suction does not have effects directly opposite to those of blowing, *e.g.* leaving unaltered $\mathcal{V}_{Q2}/\mathcal{V}_{tot}$ with respect to that of the uncontrolled case.

3.2.1. Contributions to wall-normal profiles

To characterize more precisely how pressure gradient and control strategies modify the quadrant distributions and how these changes are related to that of the turbulent statistics, we will now examine wall-normal profiles at a specific streamwise location, *i.e.* $x/c = 0.75$. This position corresponds to the center of the region for which we previously

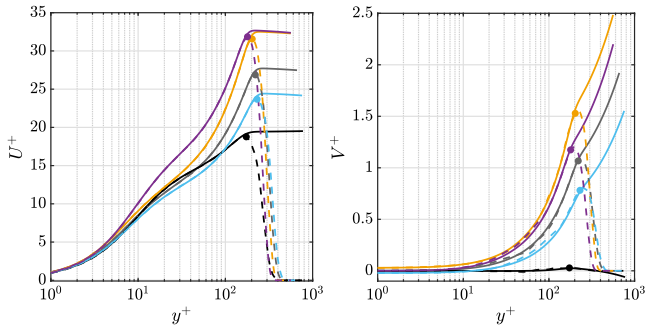

Fig. 6. Time and ensemble average, denoted by solid and dashed lines, respectively, of the (left) wall-tangential and (right) wall-normal velocity components at $x/c = 0.75$. The circle denotes the average location of the respective turbulent–non-turbulent interface (TNTI). Color code described in Table 1. (For interpretation of the references to color in this figure legend, the reader is referred to the web version of this article.)

described the probabilities of occurrence and volume fractions of the different classes of structures and quadrants.

We will firstly examine the mean properties of the flow at this location and illustrate the TNTI-condition effects. Fig. 6 shows the inner-scaled wall-tangential and wall-normal components of the time-averaged mean velocity, denoted U^+ and V^+, respectively, as functions of the inner-scaled wall-normal distance for each case at location $x/c = 0.75$. It is possible to observe (i) how the APG results in higher velocity in the wake region and much higher wall-normal convection with respect to a ZPG boundary layer, (ii) that uniform blowing increases U^+ in the wake region and wall-normal convection even further, and (iii) that suction has effects opposite to those of blowing. This Figure also shows the ensemble average of U^+ and V^+ over the snapshots employed for the coherent-structure analysis. Note that the higher V^+ in the case of body-force damping with respect to the reference is a results of the reduction of friction velocity. The outer-scaled profile of the same quantity (not shown here) is lower than in the Ref. (Atzori et al., 2021b). The ensemble average is performed only over the portion of the domain where it is possible to identify coherent structures, *i.e.* assigning a zero value to the instantaneous velocity at the location above the TNTI and in the viscous sub-layer. Thus, above δ_{99}, which provides a good estimate of the average wall-normal distance of the TNTI, the ensemble-average quantities go to zero because of the low probability that the flow is turbulent at such wall distances. Below δ_{99}, the agreement between time- and ensemble-averaged profiles is excellent for U^+ and relatively good for V^+ (the discrepancies for the latter are due to statistical uncertainty of the ensemble average).

We show the inner-scaled and outer-scaled profiles of the Reynolds stresses $\overline{u^2}$, $\overline{v^2}$, and $\overline{uv}$ for all cases in Fig. 7. The inner- and outer-scaled profiles are scaled with the squared local friction velocity, u_τ^2, and the squared local edge velocity, U_e^2, respectively. The strong adverse pressure gradient on the suction side results in more intense inner-scaled fluctuations at all distances from the wall than at the same location on the pressure side. Blowing and body-force damping exhibit even higher values than the reference case, while suction has opposite effects. These results however do not necessarily represent the absolute fluctuations intensity in different cases, because pressure gradient and control also affect the friction velocity. The outer-scaled wall-tangential fluctuations in the inner region of the boundary layer are indeed lower for the adverse pressure gradient on the suction side than on the pressure side.

It is important to point out that coherent structures are not necessarily a good indicator for the properties of the entire flow, *e.g.* if intense ejections are more common in a certain case, this does not imply that the same is true considering ejections of any amplitude. In Fig. 8, we compare the probability of belonging to each quadrant for intense events, *i.e.* when the condition $|uv| > Hu_{\mathrm{rms}}v_{\mathrm{rms}}$ is fulfilled

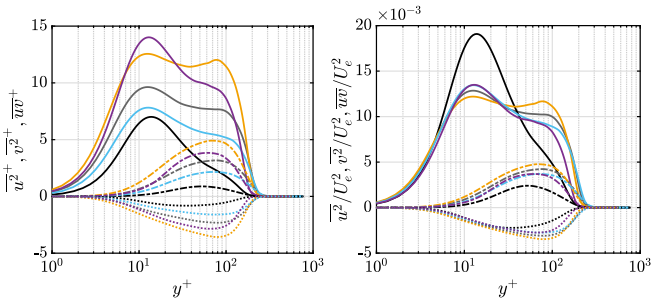

Fig. 7. (Left) Inner-scaled and (right) outer-scaled profiles of wall-tangential and wall-normal fluctuations. Solid, dashed and dotted lines denote $\overline{u^2}$, $\overline{v^2}$, and $\overline{uv}$, respectively. Color code described in Table 1. (For interpretation of the references to color in this figure legend, the reader is referred to the web version of this article.)

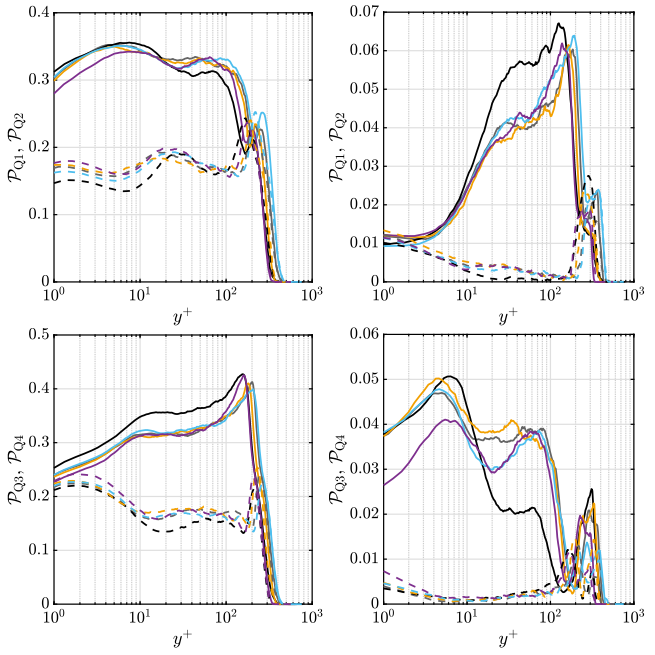

Fig. 8. Probability of belonging to different quadrants for (top row) Q1 and Q2, and (bottom row) Q3 and Q4, for (left column) the entire flow and (right column) intense events. The dominant quadrants, Q2 and Q4 are denoted by solid lines, and Q1 and Q3 are denoted by dashed lines. Color code described in Table 1. (For interpretation of the references to color in this figure legend, the reader is referred to the web version of this article.)

with $H = 2$, and the same probability in the entire turbulent flow (*i.e.* $H = 0$). The probabilities are denoted by $\mathcal{P}$ and are expressed as functions of the inner-scaled wall-normal distance (the probabilities of quadrants with the same sign of the wall-normal velocity fluctuation, *i.e.* $\mathcal{P}_{Q1}$ and $\mathcal{P}_{Q2}$, as well as $\mathcal{P}_{Q3}$ and $\mathcal{P}_{Q4}$, are shown together for the sake of clarity because they have different ranges of values). Note that the sum $\mathcal{P}_{uv} = \mathcal{P}_{Q1} + \mathcal{P}_{Q2} + \mathcal{P}_{Q3} + \mathcal{P}_{Q4}$ gives the total probability of being identified as a quadrant and part of the turbulent flow. Therefore, below $y^+ \approx 2$ and above δ_{99}, $\mathcal{P}_{uv}$ is lower than 1 even when the entire turbulent flow is considered ($H = 0$) because of the non-zero fraction of laminar flow in these regions.

For every case, $\mathcal{P}_{Q1}$ and $\mathcal{P}_{Q2}$ for $H = 0$ are qualitatively different from those of intense events only ($H = 2$). On the one hand, for $H = 0$, we observe that (i) $\mathcal{P}_{Q2}$ rapidly increases in the near-wall region, reaching its maximum at $y^+ \approx 10$, that (ii) pressure-gradient effects on this probability are relatively small, and that (iii) the most evident control effect is a reduction due to body-force damping between $y^+ \approx 1$ and $y^+ \approx 10$. On the other hand, for $H = 2$, $\mathcal{P}_{Q2}$ remains almost

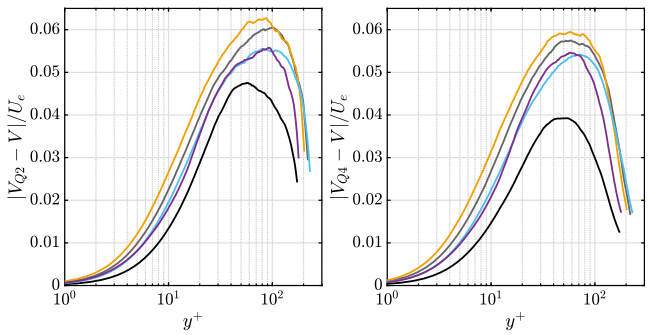

Fig. 9. Difference between the conditional averages of the wall-normal velocity for (left) ejections (Q2) and (right) sweeps (Q4) and the mean wall-normal velocity, V, scaled with the wall-tangential mean velocity at the boundary-layer edge. Note that the same scale is used for both figures, and that the region above δ_{99} is not shown. Color code described in Table 1. (For interpretation of the references to color in this figure legend, the reader is referred to the web version of this article.)

constant and very low up to $y^+ \approx 5$, it increases significantly farther from the wall, reaching its maximum in the proximity of the boundary-layer edge, and it shows a higher discrepancy between pressure and suction sides, being lower in the latter between $y^+ \approx 10$ and $y^+ \approx 100$. The probability of belonging to Q1, which is quite lower in general than $\mathcal{P}_{Q2}$, also exhibits differences between $H = 0$ and $H = 2$. In particular, in the first case, $\mathcal{P}_{Q1}$ tends to increase with the wall distance, reaching almost 25% at the edge, while in the latter one, it decreases and becomes virtually 0 far enough from the wall. The probabilities of quadrants with negative v are also different between $H = 0$ and $H = 2$. In particular, $\mathcal{P}_{Q4}$ for $H = 0$ is higher on the pressure side than on the suction side at all wall-normal distances below δ_{99}, while $\mathcal{P}_{Q4}$ for $H = 2$ is in good agreement between both in the near-wall region, and become significantly lower for the pressure side above $y^+ \approx 15$. Furthermore, $\mathcal{P}_{Q4}$ for $H = 0$ are in good agreement between reference and controlled cases, while $\mathcal{P}_{Q4}$ for $H = 2$ is lower below $y^+ \approx 10$ for body-force damping.

Overall, the differences in the quadrant probabilities between the suction and pressure sides are relatively small (at least when compared to changes seen in the turbulent statistics), but are still not negligible. In contrast, the quadrant probabilities are almost always in the very good agreement between reference and controlled cases. In fact, the most relevant control effect, which is that on $\mathcal{P}_{Q4}$ for body-force damping, is limited to a narrow near-wall region.

An interesting feature of the probabilities $\mathcal{P}_Q$ for $H = 2$ is the presence of local maxima beyond the δ_{99}, *i.e.* beyond the average TNTI, which correspond to the rare tall wall-attached events with very high y_{max} described in the previous section. We will ignore this region of the domain later on because the description of the complex dynamics of structures at the boundary between the turbulent and laminar flows is beyond the scope of the present work.

3.2.2. Structures and wall-normal convection

We will now focus on connections between intense events and wall-normal convection, which is a key feature of APG boundary layers, adopting two different perspectives, *i.e* the average intensities of these events and their contribution to the mean flow. In Fig. 9, we show the modulus of the ensemble average of the wall-normal velocity component over ejections and sweeps (denoted by V_{Q2} and V_{Q4}, respectively), minus the mean wall-normal velocity component, V, and normalized with the wall-tangential velocity at δ_{99}, denoted U_e. These conditioned averages allow a direct comparison between ejections and sweeps. Note that the normalization in outer units is employed to separate changes in the ensemble averages and friction velocity.

We observe that the ensemble averages are similar for both $Q2$ and $Q4$, although the latter are slightly lower than the former for every case. The adverse pressure gradient on the suction side has various effects. The most evident one is a higher amplitude of both ejections and sweeps, and this increase is more prominent for sweeps. In addition, the maximum of $|V_{Q2} - V|/U_e$ on the suction side is shifted farther from the wall, at $y^+ \approx 100$, while that on the pressure side is located at $y^+ \approx 50$. Both these effects concur in making the conditional average for ejections and sweeps more similar to one another on the suction side, which is perhaps surprising considering the much stronger wall-normal convection for this case.

Uniform blowing and suction result in higher and lower averaged intensities, respectively, for both $Q2$ and $Q4$, quite consistently at all wall-normal distances up to a certain location far from the wall. Beyond $y^+ \approx 100$ for uniform blowing and $y^+ \approx 150$ for uniform suction, the corresponding curves are in very good agreement with those of the reference case. Uniform blowing also moves the maxima of $|V_{Q2} - V|/U_e$ and $|V_{Q4} - V|/U_e$ closer to the wall, while suction moves them farther. This small effect is another instance of blowing and suction departing from the similarities with the adverse and favorable pressure gradients, respectively. Body-force damping modifies these quantities similarly to uniform suction but at all wall-normal distances. Note that these qualitative observations also hold for the inner-scaled conditional averages, except for body-force damping, in which case $|V_{Q2} - V|/u_\tau$ and $|V_{Q2} - V|/u_\tau$ are higher than that of the reference case (not shown here).

The conditional averages, V_Q, and the quadrant detection probabilities, $\mathcal{P}_Q$, determine the fractional contributions to the wall-normal mean velocity, denoted by $V^>$. The fractional contributions, shown in Fig. 10, are defined as the conditional averages multiplied by their respective probability of occurrence, *i.e.* $V_Q^> = \mathcal{P}_Q V_Q$. These are additive quantities, since the sum of all the contributions gives the total contribution from intense uv events, *i.e.* $V_{uv}^> = V_{Q1}^> + V_{Q2}^> + V_{Q3}^> + V_{Q4}^>$, and the difference between mean velocity and fractional contribution from intense events, $V - V_{uv}^>$, is the contribution to V from the portion of the flow not included in coherent structures.

For every case, the contributions from ejection and sweeps are by far more relevant than those from Q1 and Q3, which is a direct consequence of the low values of $\mathcal{P}_{Q1}$ and $\mathcal{P}_{Q3}$. Pressure-gradient effects are evident on both $V_{Q2}^>$ and $V_{Q4}^>$, but more significant on the latter.

The contribution of intense ejections, $V_{Q2}^>$, (which is positive) is in good agreement between suction and pressure sides up to $y^+ \approx 60$, but it becomes significantly higher for the suction side farther from the wall. This behavior is due to the changing equilibrium between probabilities of detection and intensities. The conditional average V_{Q2} is always higher on the suction side, and $\mathcal{P}_{Q2}$ is higher on the pressure side, but their relative proportion changes. On the one hand, below $y^+ \approx 60$, V_{Q2} is similar in both suction and pressure sides, and $\mathcal{P}_{Q2}$ is high enough on the pressure side so that $V_{Q2}^>$ is in good agreement between the two. On the other hand, beyond $y^+ \approx 60$, both V_{Q2} and $\mathcal{P}_{Q2}$ increase significantly on the suction side, eventually resulting in a higher fractional contribution.

The contribution of intense sweeps, $V_{Q4}^>$, (which is negative) is lower than that of ejections far from the wall in all cases, but higher near the wall, which is due to the shape of $\mathcal{P}_{Q4}$. The APG has stronger effects on $V_{Q4}^>$ than on $V_{Q2}^>$ because it increases both sweeps detection probability, $\mathcal{P}_{Q4}$, and their conditional average, V_{Q4}, of higher amounts than those of ejections, $\mathcal{P}_{Q2}$ and V_{Q2}. Subsequently, the contribution $V_{Q4}^>$ is of higher intensity for the suction side at all wall-normal distances but in particular above $y^+ \approx 10$.

The various effects on the quadrant contributions result in an interesting discrepancy between the total contributions from intense events, $V_{uv}^>$, for suction and pressure sides. This contribution is negative near the wall ($y^+ < 15$) and in good agreement between both sides because, in this region, $|V_{Q4}^>|$ is higher than $|V_{Q2}^>|$. Farther from the wall, between $y^+ \approx 15$ and $y^+ \approx 100$, $V_{uv}^>$ becomes positive for both pressure and suction sides, but it is higher for the pressure side, even though the mean wall-normal velocity is already much lower on this side.

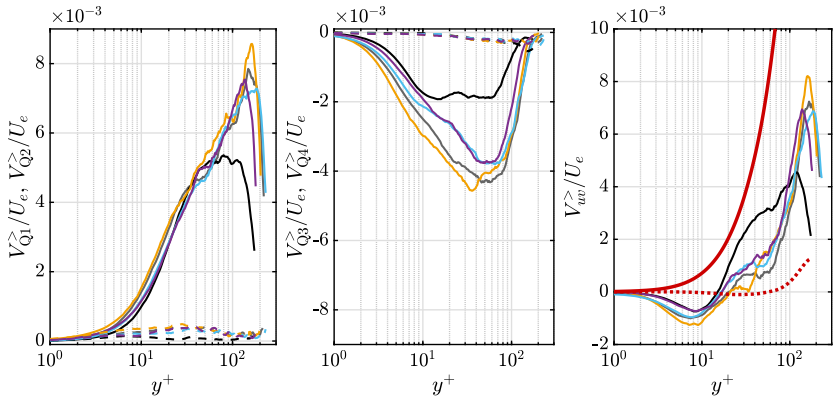

Fig. 10. Fractional contribution to the wall-normal velocity for (left) Q1 and Q2, (center) Q3 and Q4, and (right) all intense events. In the left and center figures, Q2 and Q4 are denoted by solid lines, and Q1 and Q3 are denoted by dashed lines (the range of the vertical axis is the same in both figures). In the right figure, the solid and dashed red lines denote the mean wall-normal velocity for suction and pressure sides, respectively. Note that the region above δ_{99} is not shown. Color code described in Table 1. (For interpretation of the references to color in this figure legend, the reader is referred to the web version of this article.)

Furthermore, $V^>_{uv}$ is as high as many times V for the pressure side but only a fraction of V than on the suction side. This behavior is due to the higher amplitude of the contribution from sweeps on the suction side, and it unveils a qualitative difference between ZPG and strong-APG boundary layers. In the first ones, the almost negligible wall-normal convection results from a balance between intense events and the other portion of the flow because ejections are dominant among coherent structures and $V^>_{uv}$ has high values. In the latter ones, intense sweeps reduce $V^>_{uv}$ and the portion of turbulent flows not included in coherent structures is aligned with the mean V. Even farther from the wall, for $y^+ > 100$, $V^>_{uv}$ on the suction side eventually becomes higher than that on the pressure side but remains much lower than the corresponding V.

Following the modest control effects on $\mathcal{P}_Q$ and V_Q, $V^>_{uv}$ is in relatively good agreement between the uncontrolled and controlled cases, with minor changes on the contributions. All control strategies tend to have a higher impact on $V^>_{Q4}$ than on $V^>_{Q2}$ below $y^+ \approx 100$, and $V^>_{uv}$ follows $V^>_{Q4}$. On the one hand, uniform blowing further increases $V^>_{Q2}$, and $|V^>_{Q4}|$ below $y^+ \approx 50$, decreasing $V^>_{uv}$ below $y^+ \approx 50$ and increasing it at higher wall distances. On the other hand, uniform suction and body-force damping reduce $|V^>_{Q4}|$ resulting in higher $V^>_{uv}$ in most wall-normal distances.

4. Discussion and conclusion

In the present paper, we studied coherent structures defined as intense Reynolds-stress events in the turbulent boundary layers developing on the suction and pressure sides of a NACA4412 airfoil with moderate angle of attack at $Re_c = 200,000$, including three cases with different control techniques applied on the suction side. The pressure side corresponds roughly to ZPG conditions.

The adverse pressure gradient on the suction side has many effects on coherent structures. Intense events are smaller than on the pressure side and shorter in particular, both in terms of local boundary-layer thickness and viscous length scale. Furthermore, large structures attached to the wall are less likely to appear and occupy a lower fraction of the total volume of coherent structures on the suction side. In contrast, detached structures become more common and larger. The quadrant distributions, *i.e.* the proportions of velocity fluctuations with opposite signs, are also affected by the pressure gradient. Both on suction and pressure sides, ejections are the dominant type of intense Reynolds-stress events, which is a well-known feature of wall-bounded turbulent flows. Still, they are less important in the adverse-pressure-gradient boundary layer, while sweeps become more relevant. Interestingly, the differences observed between tall-wall-attached objects and intense ejections on suction and pressure sides are more apparent in their sizes than in the probability of occurrence. This fact suggests that the pressure gradient also affects the evolution of these structures significantly.

We also found that the coherent-structure contributions to the mean wall-normal velocity component are qualitatively different between suction and pressure sides. A distinctive characteristic of adverse-pressure-gradient boundary layers is the mean wall-normal convection, which is significantly more intense than in zero-pressure-gradient cases. In the zero-pressure-gradient boundary layer, the prevalence of ejections in the outer layer leads to a positive contribution to wall-normal convection from intense events in that region. This contribution, however, is balanced by the portion of turbulent flow not included in coherent structures, resulting in low mean velocity in the wall-normal direction, similarly to channel flows. In the adverse-pressure-gradient boundary layer, fluctuations are more intense in general, but sweeps are larger and partially balance ejections. Subsequently, the contribution to wall-normal convection from structures is only a fraction of the total mean velocity, and, contrary to zero-pressure-gradients cases, the flow not included in coherent structures also gives a positive contribution to the mean.

We examined control strategies with relatively low actuation intensities, which modify the integrated skin friction by approximately 10% in the control region (the local relative change is higher closer to the trailing edge, where c_f is lower). Control effects on coherent structures are less evident than those on the turbulent statistics. This general observation is probably not surprising for uniform blowing and suction, which use a predetermined actuation, not dependent on the instantaneous flow. Similarly, although it is employed as a model for opposition control, body-force damping does not target specific events, *e.g.* with velocity fluctuations above a certain intensity or with a particular sign. Under these circumstances, control effects are mainly apparent in the mean-flow properties, and coherent structures are similar in uncontrolled and controlled cases. Nevertheless, we were able to determine that intense events are slightly shorter in the case of blowing and slightly longer for suction. Uniform blowing also increased the volume fractions of tall wall-attached structures and ejections, similarly to an even higher adverse-pressure gradient. Interestingly, uniform suction does not always have effects opposite to those of blowing, *e.g.* it reduces the volume fraction of tall wall-attached structures. Body-force damping has a very distinct impact, decreasing the volume fraction of large attached structures by an even higher amount than blowing or suction, and the probability of intense sweeps in the near-wall region.

Overall, our results show that intense Reynolds-stress events, despite the fact that they play an important role for momentum transfer and thus turbulence regeneration, are not significantly affected by predetermined control strategies, which are not specifically aimed at

modifying them. The fact that this observation holds for body-force damping as well, shows that they are also not very sensitive to modification of the near-wall region. It appears that coherent structures based on Reynolds-stress events will be significantly affected only by control strategies that target them directly, potentially employing sensors to determine when to modify the flow. Another possibility is to consider a different body-force-damping actuation targeting only fluctuations above a certain intensity. It would also be interesting to explore to what extent the control methods based on directly modifying the near-wall cycle, such as oscillating walls, affect the coherent structures.

An open question that we could not investigate is to which extent a higher Reynolds number would affect our results. On a very general point of view, the effects of both adverse pressure gradients and the control strategies that we considered become less pronounced when the Reynolds number increases and other conditions are kept constant (Vinuesa et al., 2018; Atzori et al., 2021b). This suggest that our observations on the relatively small impact on control on structures will not change. It is also reasonable to assume that structures in the outer region of the boundary layer will become progressively more relevant as the Reynolds number increases. There is however not enough data available in the literature for APG TBLs at high Reynolds number and with control, making it difficult to make hypothesis in this direction.

A second open question is how our results can be related to those using different methodologies for the study of coherent motions in wall turbulence. The sort of analysis employed here does not provide direct indications on the dynamic connections between different types of events or their evolution. Using spectral analysis to investigate the effects of blowing and suction on a similar data set but at $Re_c = 400,000$, Atzori et al. (2021b) suggested that convection of small-scale structures play an important role in increasing fluctuation intensity far from the wall. On the other hand, Fan et al. (2022), using empirical-mode decomposition (EMD (Huang et al., 1998)) on the same cases, reported that the most relevant control effects on turbulent fluctuations originate from large-scale interactions. These results suggest that it could be beneficial to focus selectively on the properties of the homogeneous-flow regions at different scales, rather than of different intensities. However, a robust definition for instantaneous large-scale or small-scale structures in the context of rapidly-evolving flow such as intense adverse-pressure-gradient turbulent boundary layers remains a challenging task. Including tracking in time in the analysis of intense events could also be beneficial (Lozano-Durán and Jiménez, 2014), but it requires *ad-hoc* implementations to avoid prohibitively high computational costs.

CRediT authorship contribution statement

Marco Atzori: Investigation, Data curation, Software, Visualization, Writing – original draft. **Ricardo Vinuesa:** Conceptualization, Methodology, Supervision, Writing – review & editing. **Philipp Schlatter:** Conceptualization, Methodology, Supervision, Writing – review & editing, Resources, Project administration, Funding acquisition.

Declaration of competing interest

The authors declare that they have no known competing financial interests or personal relationships that could have appeared to influence the work reported in this paper.

Acknowledgments

This study was funded by the Swedish Foundation for Strategic Research, project "In-Situ Big Data Analysis for Flow and Climate Simulations" (ref. number BD15-0082), by the Knut and Alice Wallenberg Foundation, Sweden and by the Swedish Research Council (VR). M.A. acknowledges financial support of the Austrian Science Fund (FWF), project number: I5180-N.

References

Atzori, M., Vinuesa, R., Fahland, G., Stroh, A., Gatti, D., Frohnapfel, B., Schlatter, P., 2020. Aerodynamic effects of uniform blowing and suction on a NACA4412 airfoil. Flow Turbul. Combust. 105, 735–759.

Atzori, M., Vinuesa, R., Lozano-Durán, A., Schlatter, P., 2019. Coherent structures in turbulent boundary layers over an airfoil. J. Phys.: Conf. Ser. 1552, 012020.

Atzori, M., Vinuesa, R., Lozano-Durán, A., Schlatter, P., 2021a. Intense Reynolds-stress events in turbulent ducts. Int. J. Heat Fluid Flow 89, 108802.

Atzori, M., Vinuesa, R., Stroh, A., Gatti, D., Frohnapfel, B., Schlatter, P., 2021b. Uniform blowing and suction applied to non-uniform adverse-pressure-gradient wing boundary layers. Phys. Rev. Fluids 6, 113904.

Bobke, A., Vinuesa, R., Örlü, R., Schlatter, P., 2017. History effects and near equilibrium in adverse-pressure-gradient turbulent boundary layers. J. Fluid Mech. 820, 667–692.

del Álamo, J., Jiménez, J., Zandonade, P., Moser, R., 2006. Self-similar vortex cluster in the turbulent logarithmic region. J. Fluid Mech. 561, 329–358.

Eto, K., Kondo, Y., Fukagata, K., Tokugawa, N., 2019. Assessment of friction drag reduction on a Clark-Y airfoil by uniform blowing. AIAA J. 57 (7), 2774–2782.

Fahland, G., Stroh, A., Frohnapfel, B., Atzori, M., Vinuesa, R., Schlatter, P., Gatti, D., 2021. Investigation of blowing and suction for turbulent flow control on airfoils. AIAA J. 59 (11), 4422–4436.

Fan, Y., Atzori, M., Vinuesa, R., Gatti, D., Schlatter, P., Li, W., 2022. Decomposition of the mean friction drag on an NACA4412 airfoil under uniform blowing/suction. J. Fluid Mech. 932, A31. http://dx.doi.org/10.1017/jfm.2021.1015.

Fischer, P., Lottes, J., Kerkemeier, S., 2008. NEK5000: Open source spectral element CFD solver. Available at: http://nek5000.mcs.anl.gov.

Huang, N.E., Shen, Z., Long, S.R., Wu, M.C., Shih, H.H., Zheng, Q., Yen, N.-C., Tung, C.C., Liu, H.H., 1998. The empirical mode decomposition and the Hilbert spectrum for nonlinear and non-stationary time series analysis. Proc. R. Soc. Lond. Ser. A Math. Phys. Eng. Sci. 454 (1971), 903–995.

Hwang, D., 2004. Review of research into the concept of the microblowing technique for turbulent skin friction reduction. Prog. Aerosp. Sci. 40, 559–575.

Kametani, Y., Fukagata, K., 2011. Direct numerical simulation of spatially developing turbulent boundary layers with uniform blowing or suction. J. Fluid Mech. 681, 154–172.

Kornilov, V., Kavun, I., Popkov, A., 2019. Modification of turbulent airfoil section flow using a combined control action. Thermophys. Aeromech. 26, 165–178.

Lozano-Durán, A., Flores, O., Jiménez, J., 2012. The three-dimensional structure of momentum transfer in turbulent channels. J. Fluid Mech. 694, 100–130.

Lozano-Durán, A., Jiménez, J., 2014. Time-resolved evolution of coherent structures in turbulent channels: characterisation of eddies and cascades. J. Fluid Mech. 759, 432–471.

Maciel, Y., Gungor, A.G., Simens, M., 2017a. Structural differences between small and large momentum-defect turbulent boundary layers. Int. J. Heat Fluid Flow 67, 95–110.

Maciel, Y., Simens, M.P., Gungor, A.G., 2017b. Coherent structures in a non-equilibrium large-velocity-defect turbulent boundary layer. Flow Turbul. Combust. 98 (1), 1–20.

Monty, J.P., Harun, Z., Marusic, I., 2011. A parametric study of adverse pressure gradient turbulent boundary layers. Int. J. Heat Fluid Flow 32, 575–585.

Park, J., Choi, H., 1999. Effects of uniform blowing or suction from a spanwise slot on a turbulent boundary layer flow. Phys. Fluids 11 (10), 3095.

Prandtl, L., 1904. Über Flüssigkeitsbewegung bei sehr kleiner Reibung. Proc. Third Int. Math. Cong. 484–491.

Skåre, P.E., Krogstad, P.m., 1994. A turbulent equilibruim boundary layer near separation. J. Fluid Mech. 272, 319–348.

Spalart, P.R., Watmuff, J.H., 1993. Experimental and numerical study of a turbulent boundary layer with pressure gradients. J. Fluid Mech. 249, 337–371.

Stroh, A., Frohnapfel, B., Schlatter, P., Hasegawa, Y., 2015. A comparison of opposition control in turbulent boundary layer and turbulent channel flow. Phys. Fluids 27, 075101.

Stroh, A., Hasegawa, Y., Schlatter, P., Frohnapfel, B., 2016. Global effect of local skin friction drag reduction in spatially developing turbulent boundary layer. J. Fluid Mech. 805, 303–321.

Vinuesa, R., Bobke, A., Örlü, R., Schlatter, P., 2016. On determining characteristic length scales in pressure-gradient turbulent boundary layers. Phys. Fluids 28, 055101.

Vinuesa, R., Negi, P., Atzori, M., Hanifi, A., Henningson, D., Schlatter, P., 2018. Turbulent boundary layers around wing sections up to $Re_c = 1,000,000$. Int. J. Heat Fluid Flow 72, 86–99.

Vinuesa, R., Örlü, R., Sanmiguel Vila, C., Ianiro, A., Discetti, S., Schlatter, P., 2017. Revisiting history effects in adverse-pressure-gradient turbulent boundary layers. Flow Turbul. Combust. 99, 565–587.

Wallace, J.M., Eckelman, H., Brodkey, R.S., 1972. The wall region in turbulent shear flow. J. Fluid Mech. 54, 39–48.

Willmarth, W.W., Lu, S.S., 1972. Structure of the Reynolds stress near the wall. J. Fluid Mech. 55, 65–92.